Three-dimensional infrared spectroscopy of isotope-diluted ice Ih

Perakis, Fivos ; Borek, Joanna A ; Hamm, Peter

Abstract: Using three-dimensional infrared (3D-IR) spectroscopy, we investigate the vibrational dynamics of isotope-diluted ice Ih. By probing the OD stretch mode of HOD in H2O, we observe an extremely rapid decay (200 fs) of the population from the second vibrational excited state. Quantum simulations based on a two-dimensional Lippincott-Schroeder potential agree nearly quantitatively with the experimental 3D-IR lineshapes and dynamics. The model suggests that energy dissipation is enhanced due to nonadiabatic effects between vibrational states, which arise from strong mode-mixing between the OD stretch mode with lattice degrees of freedom. Furthermore, we compare the simulation results to ab-initio based potentials, in which the hydrogen bond anharmonicity is too small to reproduce the experimental 3D-IR spectra. We thus conclude that the Lippincott-Schroeder potential effectively coalesces many degrees of freedom of the crystal into one intermolecular coordinate.

DOI: https://doi.org/10.1063/1.4812216

Three-dimensional infrared spectroscopy of isotope-diluted ice Ih

Fivos Perakis, Joanna A. Borek, and Peter Hamm

Citation: The Journal of Chemical Physics **139**, 014501 (2013); doi: 10.1063/1.4812216
View online: http://dx.doi.org/10.1063/1.4812216
View Table of Contents: http://scitation.aip.org/content/aip/journal/jcp/139/1?ver=pdfcov
Published by the AIP Publishing

Three-dimensional infrared spectroscopy of isotope-diluted ice Ih

Fivos Perakis, Joanna A. Borek, and Peter Hamm[a)]
Physikalisch-Chemisches Institut, Universität Zürich, Winterthurerstrasse 190, CH-8057 Zürich, Switzerland

(Received 5 April 2013; accepted 11 June 2013; published online 2 July 2013)

Using three-dimensional infrared (3D-IR) spectroscopy, we investigate the vibrational dynamics of isotope-diluted ice Ih. By probing the OD stretch mode of HOD in H_2O, we observe an extremely rapid decay (≈200 fs) of the population from the second vibrational excited state. Quantum simulations based on a two-dimensional Lippincott-Schroeder potential agree nearly quantitatively with the experimental 3D-IR lineshapes and dynamics. The model suggests that energy dissipation is enhanced due to nonadiabatic effects between vibrational states, which arise from strong mode-mixing between the OD stretch mode with lattice degrees of freedom. Furthermore, we compare the simulation results to *ab initio* based potentials, in which the hydrogen bond anharmonicity is too small to reproduce the experimental 3D-IR spectra. We thus conclude that the Lippincott-Schroeder potential effectively coalesces many degrees of freedom of the crystal into one intermolecular coordinate.
 [http://dx.doi.org/10.1063/1.4812216]

I. INTRODUCTION

Vibrational energy transfer in water is a topic that has attracted a great deal of interest in the last decades. In liquid water, it has been used to probe the hydrogen bond exchange and orientational dynamics and as such to provide microscopic insight to many physical and biochemical processes. In the mid-IR range, the OH stretch vibration is typically used to probe the local hydrogen bonding environment. The vibrational relaxation of water has been experimentally investigated by numerous pump-probe studies[1–9] assisted by simulations,[10–12] whereas the hydrogen bond exchange dynamics have been captured by photon echo and 2D-IR spectroscopy of both neat[13,14] and isotope diluted water[15–21] (see also the reviews[22–26]). Isotope dilution significantly simplifies the problem, as one can resonantly excite the OD stretch mode without exciting the OH oscillators surrounding the isolated HOD molecule. As such, one can localize the initial excitation and reduce effects arising from resonant excitation transfer.

Investigations of the vibrational energy transfer have also been extended to the crystalline phase of water with a great emphasis on ice Ih, the naturally occurring phase of the 15 different crystalline ice forms,[27] and amorphous states.[28] Ice Ih features hexagonal symmetry with respect to the oxygen lattice (symmetry $P6_3/mmc$), whereas it is disordered with respect to the hydrogen positions (proton disorder).[29] The substructure of the OH stretch mode of neat ice has been used to investigate the intra- and intermolecular coupling,[30–33] as well as the resulting vibrational exciton dynamics.[34,35] In the isotope diluted case ultrafast IR spectroscopic studies probe a 0.5 ps vibrational lifetime of the first excited state,[36–40] which is remarkably faster than that of liquid water (1 ps).[6,37] Furthermore, the temperature jump induced by the IR excitation has been shown to lead to partial melting or superheating of ice.[41]

An adiabatic approximation, similar to the Born-Oppenheimer approximation between electronic and vibrational degrees of freedom of a molecule, can often also be applied to the vibrational degrees of freedom in the electronic ground state. This is possible when a separation of timescales exists, as it frequently does between the intramolecular high frequency modes (here the OD stretch vibration) and the low-frequency intermolecular modes.[22,42] To obtain an adiabatic representation, one solves the vibrational Schrödinger equation of the high-frequency degrees of freedom for fixed values of the low-frequency degrees of freedom. This way one obtains the eigenenergies of the various vibrational states as a function of the low frequency coordinate, resulting to *vibrational adiabatic potential surfaces*. The adiabatic approximation is often very good, so that vibrational energy relaxation caused by the environment of a molecule can be treated perturbatively. Vibrational nonadiabatic effects in water have been previously suggested as possible explanations for the fast energy dissipation and hydrogen bond dissociation in liquid water and ice.[10,11] However, so far all experimental studies on water focused on energy deposited in the *first vibrational excited state* of the OH and OD stretch mode, where nonadiabatic effects are presumably quite weak.[10,11]

In this paper, we report on the observation of very strong vibrational nonadiabatic effects in isotope diluted ice Ih. Using three-dimensional infrared spectroscopy (3D-IR), we are able to directly probe the rapid energy relaxation of the *second vibrational excited state*. Qualitatively reproduced by quantum dynamics simulations based on the Lippincott-Schroeder model, the modeling suggests that energy flow is enhanced due to nonadiabatic coupling between vibrational potentials, as a result of strong mode mixing of the OD and O···O degrees of freedom. The very large nonadiabatic couplings result from the strong anharmonicity of the Lippincott-Schroeder potential. As a caveat, we present a comparison of the Lippincott-Schroeder model to *ab initio* based potentials, whose anharmonicity is too small to reproduce the

a)Electronic mail: phamm@pci.uzh.ch

experimental 3D-IR spectra, even though they partially reproduce some of the features of the Lippincott-Schroeder potential. Finally, possible solutions to resolve this discrepancy are discussed.

II. BACKGROUND

Multidimensional spectroscopy is a powerful experimental tool that provides information about the atomic motion and energy flow.[43] Realizations of such techniques, initially inspired by NMR,[44] extend over a broad spectrum of frequencies ranging from the ultraviolet to the infrared regime. Using a laser pulse sequence, one can create either a coherent superposition between states, or populate certain states and thus observe the evolution of the system. The multidimensional character permits the simultaneous creation of multiple coherence or multiple population states. In the visible frequency range realizations of three-dimensional spectroscopy feature third-order multi-coherence electronic spectroscopies,[45–47] as well the corresponding fifth-order 3D techniques.[48,49] In the infrared, three-dimensional IR spectroscopy (3D-IR) has been demonstrated as a 3-pulse 5th-order experiment exploring only coherence times,[50,51] as well as our implementation that involves five laser interactions and allows one to also observe multiple population times.[52–54]

The first experimental realization of our purely absorptive 3D-IR spectroscopy investigated the prototype example CO_2 in H_2O, which explored the contributing Liouville pathways.[52] Subsequent application of 3D-IR spectroscopy on isotope diluted liquid water focused on the lineshape of the ground state contribution, in order to extract the three-point frequency fluctuation correlation function as a function of the two population times.[54] This study suggested that liquid water exhibits heterogeneous dynamics, which originate from distinct assemblies of water molecules with a lifetime on the order of 0.5 ps.

In the current study, we explore a different feature of 3D-IR spectroscopy. Due to the larger number of pulses as compared to 2D-IR spectroscopy, 3D-IR spectroscopy climbs up higher in the vibrational ladder, which enables us to simultaneously track the dynamics of the populations for multiple vibrational states. Already from 2D-IR spectroscopy, one can access information about the $\nu = 2$ by looking at the excited state lineshape. However, the $\nu = 2$ is not actually populated but probed through its coherence with the $\nu = 1$ state, so the observed dynamics reflects the evolution of the $\nu = 1$ state (just like the $\nu = 1$ state is not populated in linear 1D spectroscopy, so any conclusion about its population relaxation is not possible). In 3D-IR spectroscopy, in contrast, one can actually populate the $\nu = 2$ state, as well as the $\nu = 1$ and $\nu = 0$ states, and observe their dynamics independently from each other as they appear as distinct spectral components in the 3D-IR spectrum.

The 3D-IR pulse sequence consist of six laser pulses (Fig. 1(a)). This configuration can be thought as an extension of 2D-IR spectroscopy by including an additional population time t_4 and coherence time t_5. The latter is responsible for the additional frequency axis ω_5. The relevant molecular response is 5th order. In 2D-IR spectroscopy exists a rephasing and a non-rephasing pathway, that need to be added up to obtain purely absorptive spectra.[55] Similarly, four such pathways exist in 3D-IR spectroscopy (R_1, R_2, R_3, and R_4).[52] These diagrams are in the same population state during t_2 and t_4 (e.g., $|0\rangle\langle 0|$ for diagram I in Fig. 1(b)), whereas they vary with respect to the sign of their coherence states. In analogy to the

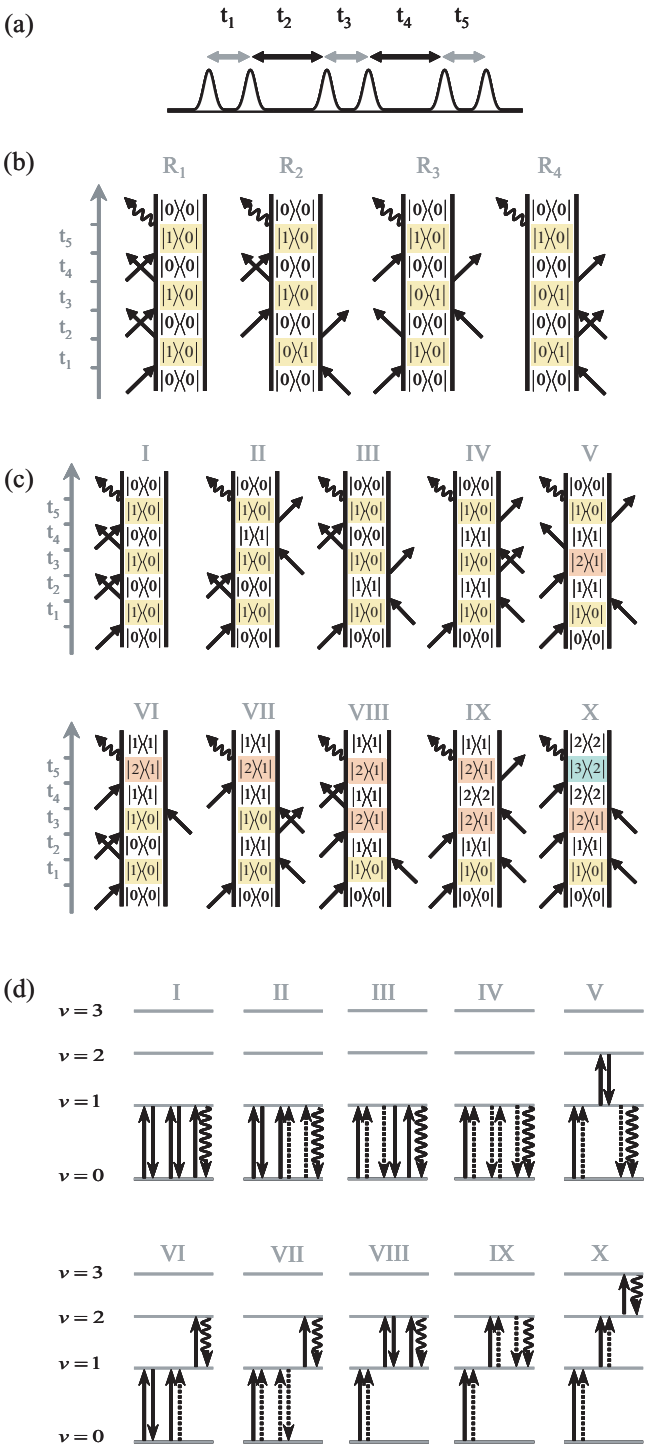

FIG. 1. (a) The 3D-IR pulse sequence: the time intervals t_1, t_3, and t_5 are the coherence times and t_2 and t_4 are the population times. (b) The four possible coherence sequences with the same population states R_1, R_2, R_3, and R_4 and (c) the ten double-sided Feynman diagrams that constitute the 3D-IR spectra in the R_1 sequence. (d) The corresponding pathways in the wave-mixing energy level (WMEL) representation.

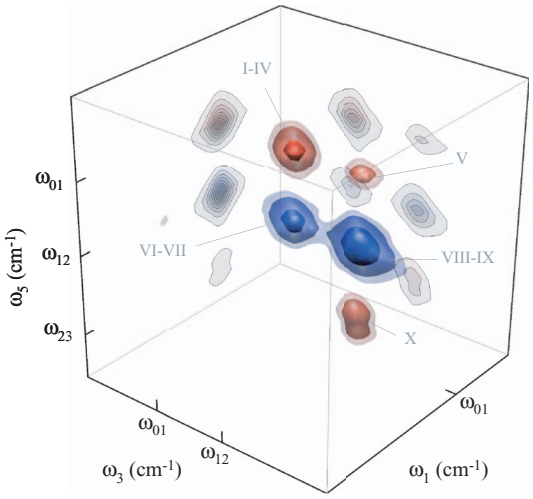

FIG. 2. 3D-IR absorptive spectrum of the prototype sample CO_2 in H_2O with the spectral positions of all the indicated diagrammatic contributions. Data similar to Ref. 52.

2D-IR case, these diagrams oscillate with $(\omega_1, \omega_3, \omega_5) = (\pm\omega_{01}, \pm\omega_{01}, \omega_{01})$, depending on whether they are in a $|0\rangle\langle 1|$ or in a $|1\rangle\langle 0|$ coherence state during t_1 and t_3.

With respect to the sequence of states during the population times, there are ten possibilities in 3D-IR spectroscopy, labeled I-X in Figs. 1(c) and 1(d). In Fig. 1(c) shows the R_1 sequence; thirty additional diagrams exist, which originate from the R_2, R_3, and R_4 sequences. To assign the 3D-IR peaks associated with each diagram, we use the spectrum of CO_2 in H_2O (Fig. 2), which is taken as a prototype example due to its nearly homogeneous lineshape.[52] Diagrams I-IV include processes that associate the ground state $|0\rangle$ with the first excited state $|1\rangle$. Since these diagrams are in $|0\rangle\langle 1|$ during the coherence times t_1, t_3, and t_5, the corresponding point in the 3D-IR spectrum is $(\omega_1, \omega_3, \omega_5) = (\omega_{01}, \omega_{01}, \omega_{01})$, as can be seen in Fig. 2. Diagram V is in a $|1\rangle\langle 0|$ state during the coherence times t_1 and t_5, and in $|2\rangle\langle 1|$ during t_3. As a result, this peak appears at $(\omega_1, \omega_3, \omega_5) = (\omega_{01}, \omega_{12}, \omega_{01})$, as shown in Fig. 2.

In a similar fashion, one can see that the diagrams VI and VII appear at frequencies $(\omega_1, \omega_3, \omega_5) = (\omega_{01}, \omega_{01}, \omega_{12})$, whereas diagrams VIII and IX appear at $(\omega_1, \omega_3, \omega_5) = (\omega_{01}, \omega_{12}, \omega_{12})$. Finally, diagram X, which is the one that creates a coherence $|3\rangle\langle 2|$, resides at $(\omega_1, \omega_3, \omega_5) = (\omega_{01}, \omega_{12}, \omega_{23})$. One can think of diagram VIII as bleaching of the first excited state, diagram IX as stimulated emission from the second excited state, and diagram X as excited state absorption of the third excited state.

Wave-mixing energy level diagrams (WMEL) are an alternative representation used to depict diagrammatically the perturbation evolution of the density matrix.[56] The information content in both formalisms is equivalent and one can translate the diagrammatic contributions between the two representations. WMEL diagrams are most commonly used to describe Raman scattering spectroscopies,[56] as well as mixed IR-VIS spectroscopies.[57,58] The advantage of using the WMEL diagrams is that representation is clearer for the case when a state (like the OD stretch here) splits to a manifold of states (as a result of coupling to the O···O vibration). Hence, we translate the double sided Feynman diagrams used in 3D-IR (Fig. 1(c)) to WMEL diagrams in Fig. 1(d).

III. MATERIALS AND METHODS

In the present section we discuss the experimental details of the 3D-IR setup, as well as the parameters and methods used in the simulations. A qualitative description is also included in Secs. VI and V, so the readers not interested in technical details can skip Sec. III.

A. Experimental methods

The experimental setup consisted of commercial Ti:Sapphire laser system which delivers pulses at $\lambda = 800$ nm of power 1 mJ at 1 kHz repetition rate. Consequently, by performing a optical parametric amplification (OPA) step, followed by difference frequency generation (DFG), we acquired mid-IR pulses of 2.5 μJ power,[59] which after precompression exhibited pulse duration of 70 fs and bandwidth of 250 cm^{-1}.

The 3D-IR setup involved 6 laser pulses in a six-wave mixing geometry.[52] The timing between these pulses was controlled by motorized translation stages as well as piezo actuators, which allowed us to individually tune the coherence (t_1, t_3, t_5) and population (t_2, t_4) time intervals. A HeNe laser beam was overlapped with the IR path and allowed us to interferometrically stabilize the coherence pulse pairs (1, 2) , (3, 4), and (5, LO) by measuring the HeNe interference patterns.[60] With the help of an active phase-stabilization scheme, we ensured that the relative phase between the pulse pairs remains constant throughout the whole measurement and the absolute phase was determined as described in Refs. 52 and 61.

The pulses were focused in the sample using the baseball diamond phase-matching geometry,[52] and the signal emitted in the direction $k_s = (k_2 - k_1) + (k_4 - k_3) + k_5$ was detected. This way, we selected the double-sided Feynman diagrams that are in a population state during the times t_2 and t_4, and in a coherence state during t_1, t_3, and t_5. The last pulse was the local oscillator (LO) with polarization perpendicular to the other pulses. Using a polarizer at 45° after the sample, the LO was overlapped with the emitted signal, where the reflected component was shifted by π with respect to the transmitted one.[62] Each component then was frequency-dispersed in a spectrometer and detected by a MCT detector with two arrays of 32 pixels each (Infrared Assoc.). Scattering contributions were suppressed by phase cycling the beam pairs (1, 2) and (3, 4) with two wobbling brewster windows (in a procedure similar to that described for 2D-IR in Ref. 63) and beam 5 with a photoelastic modulator (PEM-Hinds Instruments).

The shortest populations times chosen in this study were 100 fs, which we consider to be a compromise between minimizing pulse overlaps, that can lead to a nonresonant electronic response from the CaF_2 windows, and the need to be able to measure the very fast dynamics of the system. We did not see any significant influence on the lineshape of peak I-IV

as a function of both population times, which evidences that pulse-overlap effects are small.

For the sample, we used triply distilled H_2O and 99.9% pure D_2O in a mixture of 5%HOD in H_2O. The sample was placed between two CaF_2 widows with no spacer (estimated thickness $\simeq 1$ μm) to match the desired optical density (0.15 OD). Then it was cooled at atmospheric pressure down to 258 K using a custom made temperature-control sample holder, attached to a EtOH heat bath circulated by a chiller. The temperature was measured using a thermoresistor at the sample with ± 1 K precision.

B. Simulation methods

1. Lippincott-Schroeder potential

To model the experimental results, we employed the Lippincott-Schroeder potential,[64] which describes the hydrogen bond as a two-dimensional problem, i.e., as a function of the r_{OD} and the $R_{O\cdots O}$ coordinates (see discussion below about the validity of the model). We used the functional form,

$$V(r, R) = V_{Ia} + V_{Ib} + V_{II}, \quad (1)$$

with

$$V_{Ia} = D_{Ia}[1 - e^{-n_{Ia}(r_{OD}-r_0)^2/2r_{OD}}],$$
$$V_{Ib} = D_{Ib}[1 - e^{-n_{Ib}(R_{O\cdots O}-r_{OD}-r_0)^2/2(R_{O\cdots O}-r_{OD})}],$$
$$V_{II} = D_{II}[1 - e^{-n_{II}(R_{O\cdots O}-R_0)}]^2,$$

where r_0 is the equilibrium distance, taken from the O-D length in the gas phase. The terms V_{Ia} and V_{Ib} describe the interaction between the proton and the two oxygens, with binding energy D_{Ia} and D_{Ib} correspondingly. Additionally, the term V_{II} includes a Morse interaction between the two oxygens with an equilibrium distance R_0. The parameters used, taken from Refs. 38 and 40, are summarized in Table I.

2. Ab initio based potentials

The Lippincott-Schroeder potential was compared to *ab intio* based potentials, using the same two coordinates r_{OD} and $R_{O\cdots O}$. To that end, we considered a water dimer $(H_2O)_2$ both in vacuum and in the environment of an ice Ih crystal. In the vacuum case, we calculated the potential energy surface on the MP2/aug-cc-pVTZ level of theory[65] and using a parameterized potential made available by Bowman and coworkers,[66,67] which has been fitted to CCSD(T)/aug-cc-pVTZ calculations (that potential was also recently applied to simulate the FT-IR spectra of neat ice[68]). We started from a minimized configuration of the water dimer and varied the r_{OD} and $R_{O\cdots O}$ distances, keeping all other coordinates fixed. In order to capture also the polarization effects that potentially could stabilize an auto-ionized state, which is an important ingredient of the Lippincott-Schroeder potential, we extended the simulations to an ice Ih crystalline cluster of 34 water molecules, using the Bowman potential. The crystalline cluster was constructed around a central dimer placed along the crystal c-axis (perpendicular to the basal plane 0001), with two successive solvation shells. The outer solvation shell was fixed in order to impose the crystal environment, whereas the configuration of the waters of the inner shell was energy-minimized for every point in (r_{OD}, $R_{O\cdots O}$) space, in order to mimic the lattice distortion and overall orientational polarizability. During energy minimization, the (r_{OD}, $R_{O\cdots O}$) distances were constrained using SHAKE,[69] but all other degrees of freedom of the water dimer and the first solvation shell were allowed to vary.

TABLE I. The parameters of the Lippincott-Schroeder model for ice Ih, as taken from Refs. 38 and 40.

$D_{Ia} = 38750$ cm^{-1}	$n_{Ia} = 10.0$ Å^{-1}	$r_0 = 0.97$ Å
$D_{Ib} = 25000$ cm^{-1}	$n_{Ib} = 16.5$ Å^{-1}	$R_0 = 2.88$ Å
$D_{II} = 2000$ cm^{-1}	$n_{II} = 2.9$ Å^{-1}	

3. Vibrational eigenstates

For a numerical solution of the 2D vibrational Schrödinger equation, we used a sinc-function discrete variable representation (DVR) basis in cartesian coordinates,[70] with an equally spaced grid properly centered with spacing 0.04 Å along the r_{OD} and 0.07 Å along the $R_{O\cdots O}$ coordinate (chosen such that the relevant bound eigenstates are converged). The kinetic energy operator was assumed to be decoupled for the two coordinates, with effective masses $\mu_{OD} = 2$ and $\mu_{O\cdots O} = 9$ (i.e., two water molecules with mass 18). Diagonalizing the resulting Hamiltonian matrix, we obtained all eigenstates with corresponding wavefunctions. Additionally, the transition dipoles between each pair of states i and j could be calculated

$$\mu_{ij} \propto \langle \phi_i | r_{OD} | \phi_j \rangle, \quad (2)$$

where we assume that only the polar OD group contributes.

We then selected eigenstates that participate to a particular Feynman diagram, referred to as *bright states* (Fig. 4(b)). We exemplify the method of choosing bright states for diagram IX (Fig. 1(c)). As we examined a low-temperature limit, the initial state was the ground state at 0 cm^{-1} (zero point energy subtracted). Even though consideration of the thermal occupation of the ground state manifold at the experimentally performed temperature could potentially bring the simulations even closer to the experiment, due to the low dimensionality of the model the density of the lower eigenstates is captured only qualitatively and as a result the temperature effect does not make any significant difference. That is, in the framework of the model, the first excited state has energy 400 cm^{-1}, which corresponds to a temperature of 576 K and as such it does not contribute to the calculated response. By calculating μ_{ij} from $i = 0$ to $j = j_{max}$ (where $j_{max} = 100$ is the maximum number of participating eigenstates), we defined the $\nu_{OD} = 1$ manifold. To that end, we applied a bandwidth restriction to mimic the pulse bandwidth (1000 cm^{-1}), and we reduced the number of states for computational purposes by keeping only states above a certain cutoff value of μ_{ij} (tested for convergence). Similarly, calculating the μ_{ij} between the states of the $\nu_{OD} = 1$ manifold and all the higher states allowed us to define the $\nu_{OD} = 2$ manifold. Finally, as can be seen from Fig. 1(c) (and the corresponding WMEL diagrams in

Fig. 1(d)), diagram IX returns to the $\nu_{OD} = 1$ manifold. By calculating μ_{ij} between the states involved in manifold $\nu_{OD} = 2$ and all the lower states, with the application of the aforementioned restrictions, the manifold $\nu_{OD} = 1$ was extended. Similarly in diagram X, this last step defines the $\nu_{OD} = 3$ manifold. This method produces a different number of states participating in each diagram during the various time intervals.

4. Diagrammatic perturbation theory

To simulate the 3D IR spectra, we used diagrammatic perturbation theory,[43,71] including all bright states in each diagram. The 5th order response functions $R^{(5)}$ originating from each diagram have the general form

$$R^{(5)}(t_1, t_2, t_3, t_4, t_5) = (-1)^n \sum_{states} M \cdot e^{i \cdot a(t_1,t_2,t_3,t_4,t_5)} \cdot g(t_1, t_3, t_5), \quad (3)$$

where n is the number of interactions on the *ket* (which is responsible for the final sign of each diagram encoded in red/blue in Figs. 2, 3, 5, and 6), M is the product of the transition dipoles of each pulse interaction, $a(t_1, t_2, t_3, t_4, t_5)$ the time evolution of the density matrix during each time interval and $g(t_1, t_3, t_5)$ the 3D lineshape function. For example, the aforementioned functions participating in diagram R_X are

$$M_X = \mu_{01}(0, i) \cdot \mu_{01}(0, j) \cdot \mu_{12}(i, k) \cdot \mu_{12}(j, l) \cdot \mu_{23}(k, m) \cdot \mu_{23}(l, m),$$

where μ_{01}, μ_{12}, and μ_{23} are the transition dipole matrices between manifolds $\nu_{OD} = 1$, 2, and 3, and the corresponding summation indexes (i, j, k, l, m) refer to the bright states of each manifold. The time evolution component for diagram R_X is

$$\begin{aligned} a_X(t_1, t_2, t_3, t_4, t_5) = & -\omega_1(i)t_1 \\ & + [-\omega_1(i) + \omega_1(j)]t_2 \\ & + [-\omega_2(k) + \omega_1(j)]t_3 \\ & + [-\omega_2(k) + \omega_2(l)]t_4 \\ & + [-\omega_3(m) + \omega_2(l)]t_5, \end{aligned}$$

where the $\omega_k(i)$ correspond to the frequency of state i of the manifold $\nu_{OD} = k$. The sign of each term reflects whether the interaction is with the *ket* $(-)$ or with the *bra* $(+)$.

Finally, as phenomenological lineshape function $g(t)$, which we assumed to be the same for all diagrams, we have chosen a Lorentzian profile

$$g(t_1, t_3, t_5) = e^{-(t_1+t_3+t_5)/T_2} \quad (4)$$

with a homogeneous dephasing time $T_2 = 0.2$ ps. Additionally, the Fourier transform along the coherence times was apodized with a Gaussian window function chosen to facilitate the comparison between experiment and theory. No phenomenological relaxation term T_1 was included for the population times t_2 and t_4, so any dynamics observed as a function of the population time reflect the inherent time evolution of the wavepacket.

IV. EXPERIMENTAL RESULTS

The experimental 3D-IR spectra of the OD stretch vibration of HOD in H_2O ice Ih at T = 258 K are presented in Fig. 3. For early population times $(t_2, t_4) = (100$ fs, 100 fs) four distinct peaks are observed. These peaks exhibit not only variation in the signal strength but also with respect to their lineshape along the three axes's. That is, the bandwidth of peak that arises from contributions I-IV is comparable to that of the linear spectrum, with a bit of elongation along the body diagonal, as can be seen in the projections onto the (ω_1, ω_5) and (ω_3, ω_5) planes. We associate this characteristic with inhomogeneous broadening due to proton disorder. This feature, which has been observed also in our previous 2D-IR study,[40] stays constant for the observed timescale as the reorganization of protons in ice are known to be much slower[72] and as such does not lead to spectral diffusion within the timescales of the experiment. Peaks V and VI-VII, in contrast are elongated along ω_3 or ω_5, respectively, whereas peak VIII-IX is elongated along *both* ω_3 and ω_5. This lineshape asymmetry between ground and excited state contributions has been previously observed in the pump-probe response of liquid water and ice[36,38] and has been shown to depend on the hydrogen bond strength.[73] Finally, we do not observe peak X within the signal-to-noise ratio of the experiment.

Figures 3(b) and 3(c) follow the dynamics of the 3D-IR spectra as a function of the second population time t_4. Peaks I-IV, V, and VI-VII stay almost constant, whereas peak VIII-IX vanishes within 200 fs. The volume (integrated intensity at FWHM) of the observed peaks as a function of t_4 is presented in Fig. 3(d). Despite the limited number of time points, one can conclude that peak VIII-IX decays much more rapidly than the remaining ones. Even though the latter peak does seem to vanish in the 3D-IR spectrum due to the choice of the 3D contours, in reality it does not decay completely, as can be seen by the corresponding projection on the (ω_3, ω_5) plane, as well as from the integrated volume in Fig. 3(d).

V. SIMULATION RESULTS

A. Vibrational eigenstates

We discuss the underlying physical mechanism responsible for the peculiar lineshapes of the 3D-IR spectra and their dynamics on the basis of the Lippincott-Schroeder model.[64] The Lippincott-Schroeder potential is an empirical model of the hydrogen bond potential, which includes two relevant degrees of freedom: the O–H intramolecular distance r_{OH} (or r_{OD} in our case since we work with isotope diluted water) of the hydrogen bond donor and the O···O intermolecular distance $R_{O\cdots O}$ of the two waters that are hydrogen bonded (Fig. 4(a)). The Lippincott-Schroeder potential has been used before to simulate IR pump-probe and 2D-IR spectra of liquid water[74] and of ice[38,40] and more recently to describe the vibrational dynamics in DNA.[75] The model idealizes the problem to a water dimer, a treatment which can be partially justified

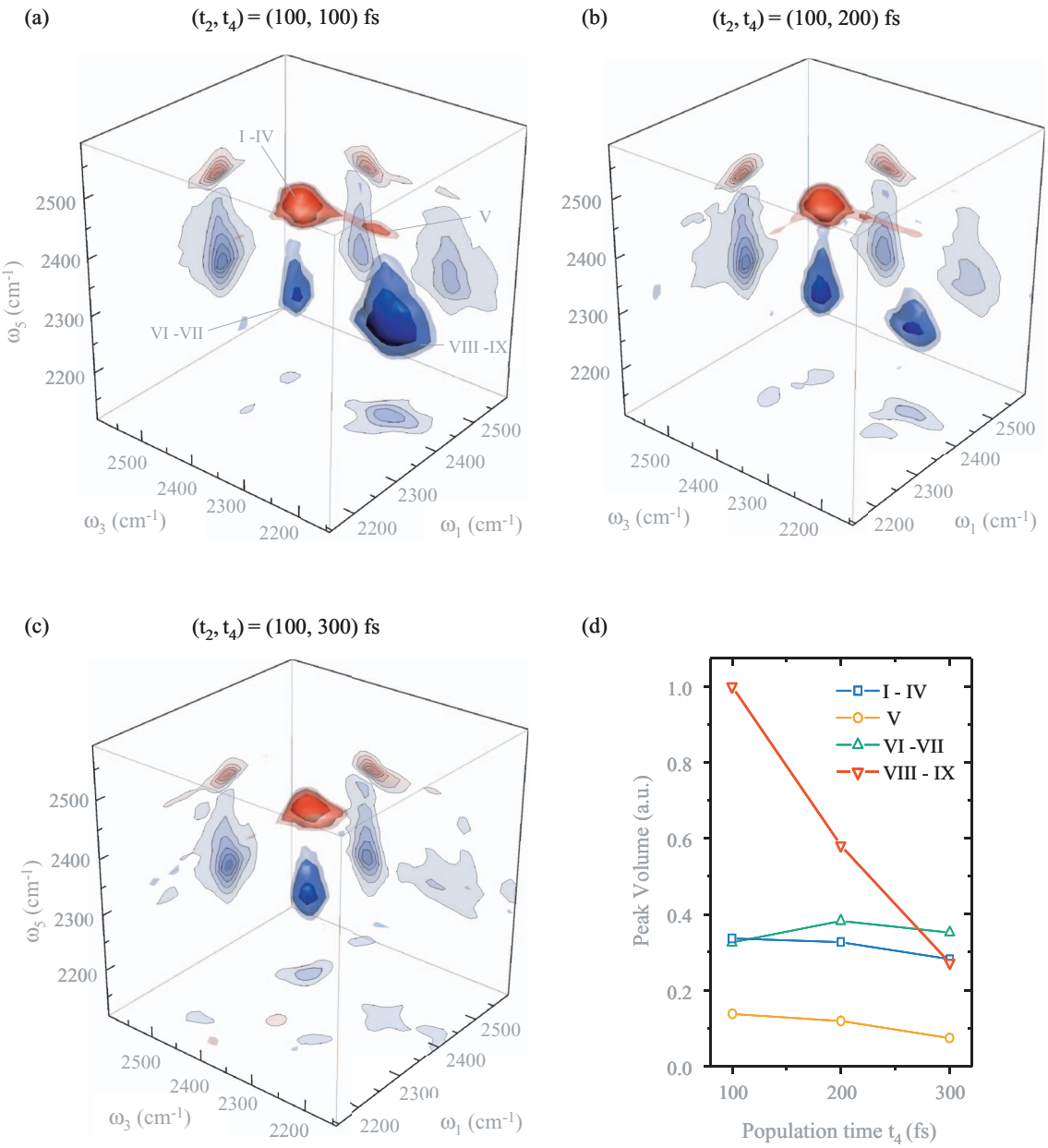

FIG. 3. (a)–(c) Experimental 3D-IR spectra of the OD stretch of isotope diluted ice Ih (5% HOD/H_2O) at different population times (t_2, t_4). (d) The peak volume (integrated intensity) of each of the observed peak as a function of t_4 for $t_2 = 100$ fs.

by the local character of the excitation due to isotope diluting in our experiment. In addition, it assumes that we excite a single longitudinal phonon through a Franck-Condon like transition, similar to the case of small molecules in rare gas matrices, where the electronic excitation induced initially localized coherent zone boundary phononic oscillations.[76] Nevertheless, we interpret the simulation results on a qualitative level and do not attempt to fit parameters to the experimental results, but instead use a previous parametrization.[38] As we will see, this level of theory appears to be sufficient to describe the experimental observations almost quantitatively.

By solving the vibrational time-independent Schrödinger equation on the 2D Lippincott-Schroeder potential with coordinates r_{OD} and $R_{O\cdots O}$, the spectrum of eigenstates shown in Fig. 4(b), left column, is obtained. A selection of the corresponding wavefunctions is shown in Fig. 4(c). Observing the nodal lines in these wavefunctions, one can assign the corresponding states. Lower energy states can be characterized as vibrational ground state (ν_{OD}, $\nu_{O\cdots O}$) = (0, 0) at 0 cm^{-1} (zero-point energy subtracted), or as excited with one quantum along the $R_{O\cdots O}$ coordinate (ν_{OD}, $\nu_{O\cdots O}$) = (0, 1) at 400 cm^{-1} or one quantum along the r_{OD} coordinate (ν_{OD}, $\nu_{O\cdots O}$) = (1, 0) at 2240 cm^{-1}, respectively. For higher excited states, *mode mixing* becomes relevant (where the term mode mixing refers to the sum of product states and not just to combination modes). For example, the 2660 cm^{-1} state is still predominantly a product state (combination mode) with (ν_{OD}, $\nu_{O\cdots O}$) = (1, 1), but already contains a small contribution from (ν_{OD}, $\nu_{O\cdots O}$) = (0, 13). In this energy regime, coupling is still weak so the amount of mode mixing depends on accidental resonances. But mode mixing becomes very strong for higher states (4180 cm^{-1}, 5295 cm^{-1}), where it is no longer possible

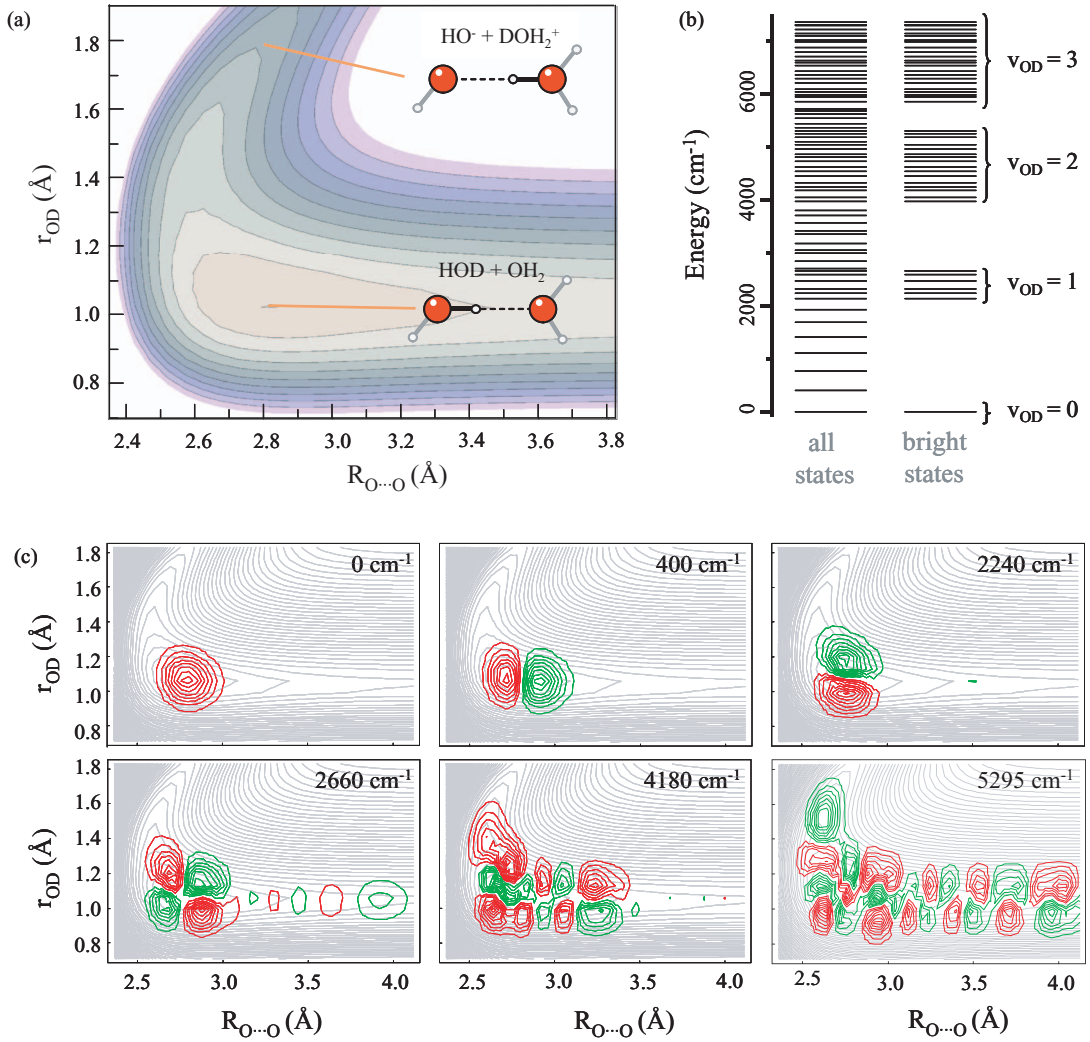

FIG. 4. (a) Lippincott-Schroeder potential as a function of the intramolecular OD and the intermolecular O···O distances. (b, left) Spectrum of all eigenstates and (right) of the bright states that contribute to the 3D-IR spectra. (c) A few typical vibrational wavefunctions at the energies indicated.

to unambiguously assign quantum numbers for the two degrees of freedom. The density of states and the coupling is so high in this regime that mode-mixing does no longer depend on accidental resonances but will always occur.

Calculating the transition dipole moments, Eq. (2), we can select the bright states within the various ν_{OD} manifolds (Fig. 4(b), right column, see Sec. III for details of the procedure). The various ν_{OD} states split into *manifolds* due to contributions from O···O modes. They become increasingly richer as one climbs higher in the vibrational ladder due to an increasing density of states and mode mixing. As we will see, this splitting into manifolds can explain the experimentally observed lineshape features as well as the kinetics of the various 3D-IR peaks.

B. Simulated 3D-IR spectra

The 3D-IR spectra were simulated using the diagrammatic perturbation theory, as detailed in Sec. III. The simulations allow us to disentangle overlapping diagrams, so we examine them separately in order to unravel the origin of the 3D-IR lineshape distortion. The left-hand sides of Figs. 5(a)–5(d) shows the WMEL diagrams V, VIII, IX, and X with the corresponding bright states during each time interval. The right-hand sides shows the corresponding purely absorptive 3D-IR spectra.

Diagrams V and VIII are identical during the first four field interactions. Starting from the ground state $|0\rangle\langle 0|$, the first two laser pulses at $t = 0$ and t_1 promote the system into the $\nu_{OD} = 1$ manifold, which consist of three bright states. The subsequent pulse generates a coherence between the $\nu_{OD} = 1$ and the $\nu_{OD} = 2$ manifolds, the latter of which is richer in number of bright states, resulting in the elongation of the peaks along ω_3. After the coherence time interval t_3, the system returns back to the $\nu_{OD} = 1$ manifold. Since the system has explored more pathways by that time as compared to t_1, more states in the $\nu_{OD} = 1$ manifold are now involved. With the 5th laser pulse, diagrams V and VIII separate. While diagram V returns back to the ground state ($\nu_{OD} = 0$) through stimulated emission, diagram VIII once again explores the $\nu_{OD} = 2$ manifold. The even larger number of bright states involved in this step results in further broadening of the $\nu_{OD} = 2$ manifold, which manifests as additional elongation of peak VIII along ω_5.

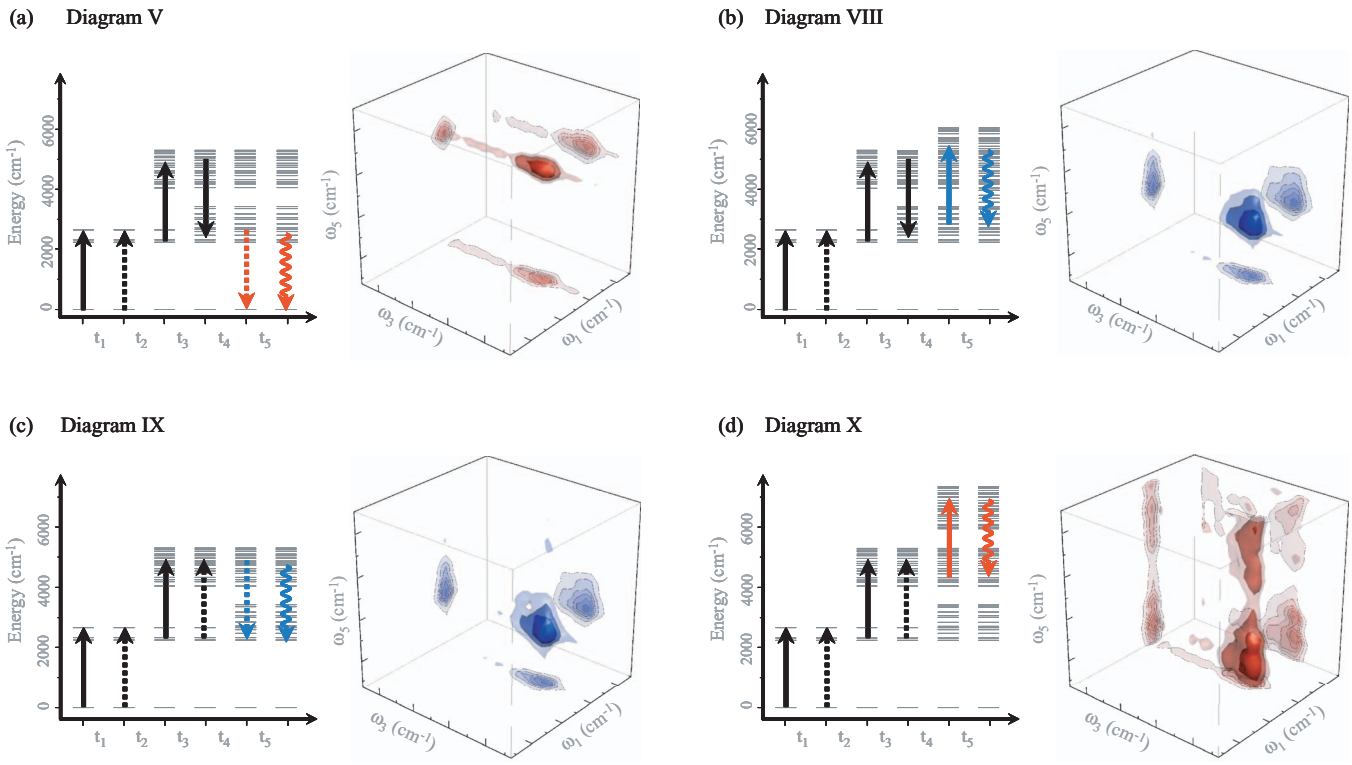

FIG. 5. (a)–(d) Simulated 3D-IR spectra for individual WMEL diagrams. Population times are $t_2 = t_4 = 0$.

Diagrams IX and X are discussed in a similar fashion. Diagram IX passes from the $\nu_{OD} = 1$ to a population in the $\nu_{OD} = 2$ manifold during t_3, which results in elongation of peak IX along ω_3. During t_5 the transition from the $\nu_{OD} = 2$ manifold back to the $\nu_{OD} = 1$ leads to elongation of peak IX along ω_5. Peak X appears much broader than all other peaks, as a result of the transition during t_5 from manifold $\nu_{OD} = 2$ to $\nu_{OD} = 3$. The oscillator strength of the particular contribution is distributed over a very broad range, and in fact results in a double peak along ω_5 (Fig. 5(d)), which originates from pathways that end up in the $\nu = 1$ instead of the $\nu = 2$ manifold of states, indicating that a clear distinction between $\nu_{OD} = 1$ and $\nu_{OD} = 2$ is no longer possible in this case.

The complete 3D-IR lineshape (Fig. 6(a)) can be obtained by adding up all diagrammatic contributions. Despite the simplicity of our model, we observe surprisingly good agreement with the experiment (Fig. 3(a)). All lineshape features are reproduced almost quantitatively. That is, peak V is elongated along ω_3 axis just like in the experiment, peak VI-VII along ω_5 and peak VIII-IX along both ω_3 and ω_5. Peak X is very weak as the oscillator strength is distributed over a very wide range and overlaps with peaks V and VIII-IX; as such it is not visible with the contour surfaces chosen for the representation of the 3D-IR spectra in Fig. 6, except from traces that can be identified in the (ω_1,ω_5) and (ω_3,ω_5) projections. The weak intensity of peak X could explain why we cannot resolve it within the signal-to-noise of the experiment. Finally, since our model does not include any inhomogeneity due to proton disorder, peak I-IV does not exhibit the body-diagonal elongation observed in the experiment.

The model is not only capable to explain the line shapes of the various 3D-IR peaks, but also their dynamics. Figure 6(b), solid line, shows the integrated volume (up to the FWHM) of peak VIII-IX as a function of t_4, which is the one that exhibits the experimentally observed rapid decay. Once again, the simulation compares quite well with the experiment (Fig. 3(d)) and reproduces the observed rapid decay of peak VIII-IX. In the simulation, we can disentangle the overlapping contributions from diagrams VIII (dotted line) and IX (dashed line), which probe the evolution of the $\nu_{OD} = 1$ and $\nu_{OD} = 2$ manifolds of states, respectively, as a function of t_4. Interestingly, the population from the $\nu_{OD} = 2$ has decayed almost completely within the observed time window, whereas that of $\nu_{OD} = 1$ stays almost constant. Consequently, peak VIII-IX decay to half its initial intensity Fig. 6(b), whereas the corresponding decay in the experimental data is larger (Fig. 3(d)). That discrepancy could be due to the fact that diagram VIII has already populated the $\nu_{OD} = 1$ state during the time interval t_2 (and the same is true for diagram V). As such, in these diagrams the manifold of the population in the $\nu_{OD} = 1$ state has already experienced a decay during t_2, making the corresponding response weaker. This additional $\nu_{OD} = 1$ decay is not the part of the model. It could be due to additional vibrational relaxation pathways such as the HOD bending vibration, which was shown to contribute significantly in the case of isotope diluted water.[5,9,10,77] Even though such an extension of the model would be particularly informative concerning the additional coupling to intramolecular degrees of freedom, goes beyond the scope of the present study.

The fast relaxation of the $\nu_{OD} = 2$ state could also be estimated from a harmonic scaling relation for the vibrational

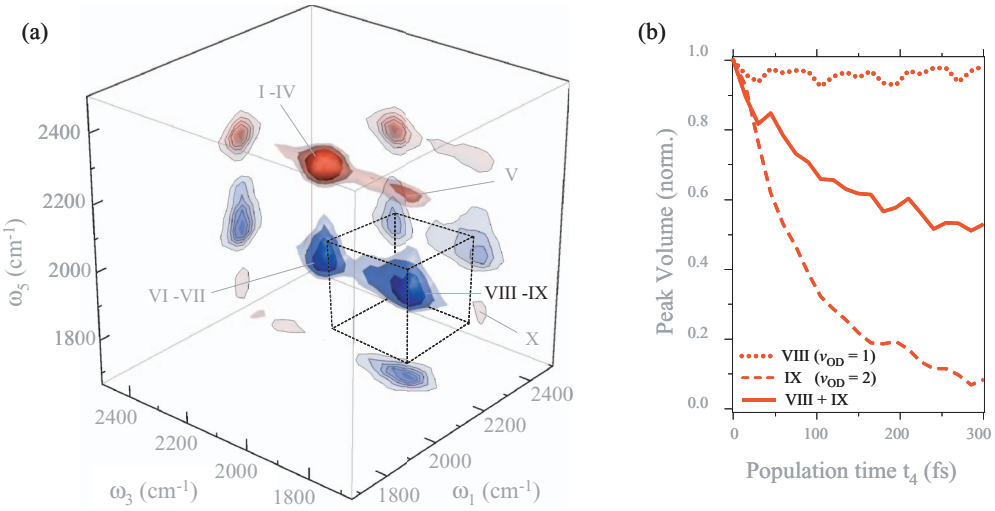

FIG. 6. (a) Complete simulated 3D-IR spectrum with all diagrams added for $t_2 = t_4 = 0$ and (b) simulated integrated intensity of diagrams VIII and IV as a function of t_4 with $t_2 = 0$.

lifetime, which would decrease by a factor of 2 compared to the $\nu_{OD} = 1$ decay, which in turn has been measured to be 0.5 ps.[36–40] However, within the framework of the model, such a perturbative treatment is no longer adequate, as seen for example from the difference in the decay of peaks VIII and IX ($\nu_{OD} = 1$ and $\nu_{OD} = 2$, respectively) in Fig. 6(b).

Recurrences of the $\nu_{OD} = 2$ state are observed at later population times (not shown in Fig. 6(b)), which are attributed to the finite number of states involved in the model. Note that no phenomenological T_1 relaxation term has been added to the response functions in Eq. (3), but the rapid decay is intrinsic to the time-evolution of quantum system. As discussed in Sec. V C, it is the nonadiabatic couplings between the $\nu_{OD} = 2$ and lower vibrational states, which facilitate population relaxation.

C. Vibrational nonadiabatic effects

The origin of the rapid energy dissipation through the $\nu_{OD} = 2$ state becomes clear in a wavepacket representation (Fig. 7(a)). To that end, we idealize diagram IX and prepare an impulsively excited wavepacket in the $\nu_{OD} = 2$ state by considering all pathways over bright eigenstates in the $\nu_{OD} = 1$ manifold into those in the $\nu_{OD} = 2$ manifold, scaled by the corresponding transition dipoles μ_{0i} and μ_{ij}, respectively, of the two steps:

$$|\Phi_2(r, R, t = 0)\rangle = \sum_i^{n_1} \sum_j^{n_2} \mu_{0i} \cdot \mu_{ij} |\varphi_j(r, R)\rangle. \qquad (5)$$

Here, i labels all states in the $\nu_{OD} = 1$ manifold, j those in the $\nu_{OD} = 2$ manifold and $|\varphi_j(r, R)\rangle$ are the eigenstates in the $\nu_{OD} = 2$ manifold. The impulsively excited wavepacket features two vibrational quanta in the r_{OD} coordinate without any excitation or displacement in the $R_{O\cdots O}$ coordinate (Fig. 7(a), 0 fs panel). We get an excitation exclusively in the r_{OD} coordinate, because we had defined the transition dipole along that coordinate (Eq. (2)). In other words, the initially excited state is a zero-order state defined through its transition dipole,[78] but it is *not* an eigenstate of the system. As such, the impulsively excited wavepacket will propagate in time,

$$|\Phi_2(r, R, t)\rangle = \sum_i^{n_1} \sum_j^{n_2} \mu_{0i} \cdot \mu_{ij} |\varphi_j(r, R)\rangle e^{-i\frac{\epsilon_j}{\hbar}t}, \qquad (6)$$

where ϵ_j is the energy of the corresponding eigenstate. The result of that time-propagation is shown in Fig. 7(a). At early

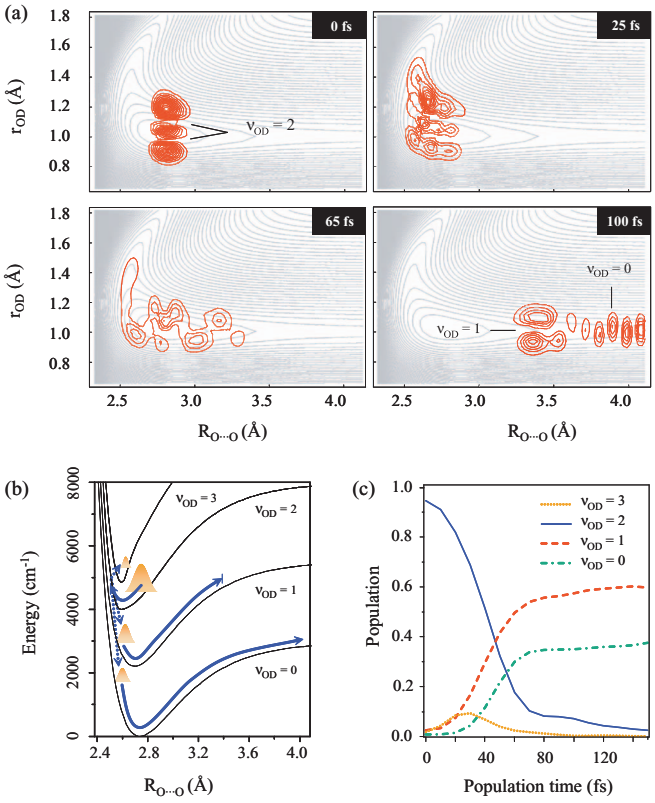

FIG. 7. (a) Time-propagation of an impulsively generated wavepacket on the $\nu_{OD} = 2$ state in a full 2D representation. (b) Vibrationally adiabatic surfaces with the time-propagation of the wavepacket indicated. (c) Populations of the wavepacket projected onto the different adiabatic states.

times (40 fs) the wavepacket moves to lower $R_{O\cdots O}$, followed by subsequent spreading of the wavepacket (65 fs) and eventually propagation to longer $R_{O\cdots O}$ (100 fs). At that time, the wavepacket is split into one fraction that features one quantum in the r_{OD} coordinate and that evolves out to 3.5 Å from where it returns to shorter $R_{O\cdots O}$ in an oscillatory fashion. The second fraction features zero quanta in the r_{OD} coordinate and continues to evolve to longer $R_{O\cdots O}$ distances (it would in fact dissociate if our simulation box wouldn't be finite).

The more conventional picture of the same process is obtained in an adiabatic representation. The adiabatic approximation is motivated by the timescale separation between intramolecular OD vibration and intermolecular O···O vibration. To obtain the adiabatic representation, one solves the 1D Schrödinger problem of the r_{OD} coordinate for fixed $R_{O\cdots O}$ distances, resulting in energies of the various ν_{OD} states that depend parametrically on $R_{O\cdots O}$. Repeating that for all $R_{O\cdots O}$'s, one can assemble vibrational potential energy surfaces for the various ν_{OD} states as a function of $R_{O\cdots O}$ (Fig. 7(b)). These vibrational potential energy surfaces are displaced with respect to each other, become more anharmonic as one climbs up the ν_{OD} ladder and feature increasing dissociation energies. The shift of the minimum of the potential energy surfaces towards shorter $R_{O\cdots O}$ distances reflects the well-known fact that excitation of the OD stretch vibration results in a shorter and stronger hydrogen bond.[10]

The procedure described above for the impulsive excitation of a $\nu_{OD} = 2$ wavepacket (Eq. (5)) is equivalent to the common Franck-Condon picture, according to which the ground state wavepacket is projected vertically onto the $\nu_{OD} = 2$ potential energy surface. Since that potential energy surface is displaced, the wavepacket is no longer in equilibrium and will start to propagate. If the adiabatic approximation would be valid, it would start to oscillate on the $\nu_{OD} = 2$ potential energy surface. What happens, however, is that the wavepacket crosses to the $\nu_{OD} = 1$ and $\nu_{OD} = 0$ potential energy surfaces at the left turning point of the $\nu_{OD} = 2$ potential energy surface. This is quantified in Fig. 7(c), where the projection of the exact solution, Eq. (6), (Fig. 7(a)) onto the adiabatic potential energy surfaces (Fig. 7(b)) is shown. In this way one can acquire the population of the various ν_{OD} states as a function of time. The $\nu_{OD} = 2$ state (blue solid line) is very rapidly depopulated within half an oscillation period, with a corresponding rise in the $\nu_{OD} = 1$ and $\nu_{OD} = 0$ populations. The $\nu_{OD} = 3$ state is also transiently populated for a short time (dotted orange line). We consider that feature to be more a manifestation of the breakdown of the adiabatic approximation in this energy regime rather than an experimental observable. The energy of the resulting $\nu_{OD} = 1$ wavepacket is not sufficient to overcome the corresponding dissociation energy, so it remains oscillatory, but the $\nu_{OD} = 0$ wavepacket does have sufficient energy, so it could in fact break the hydrogen bond.

The rapid drop of $\nu_{OD} = 2$, and thus the decay of diagram IX and the corresponding peak in the 3D-IR spectrum, is the result of an essential breakdown of the adiabatic approximation for the $\nu_{OD} = 2$ state. Repeating the same procedure for an impulsively excited $\nu_{OD} = 1$ wavepacket shows in accordance with earlier work[10,11] that the adiabatic approximation is still very good in this case, so the wavepacket is oscillatory with hardly any relaxation into the $\nu_{OD} = 0$ state (results not shown).

Comparison of the full 2D wavepacket propagation of Fig. 7(a), which implicitly includes all nonadiabatic couplings, with the adiabatic representation of Figs. 7(b) and 7(c) shows that mode mixing in the full 2D representation is the equivalent to nonadiabatic couplings in the adiabatic representation. Eigenstates in the energy regime of the impulsively excited wavepacket are strongly mode mixed, as shown in Fig. 4(c). Hence, if one expands that wavepacket, which looks like an exclusive OD excitation, in a basis of eigenstates that have character of all possible OD excitations, it will eventually evolve into all these states.

VI. DISCUSSION AND CONCLUSION

In this paper, we apply 3D-IR spectroscopy to the OD vibration of isotope diluted ice Ih, making use of the fact that 3D-IR spectroscopy climbs higher in the vibrational ladder than previous studies and thus explores more of the anharmonicity of the hydrogen bonds potential. In particular, 3D-IR spectroscopy actually *populates* the second excited state of the OD vibration, while 2D-IR or IR pump-probe spectroscopy, which has been used extensively to study water in its liquid and crystalline form, probes the second excited state only through its coherence with the first excited state.

We find that quantum-dynamics simulation based on a 2D Lippincott-Schroeder potential can almost quantitatively reproduce the experimental 3D-IR results, both in terms of the 3D-IR lineshape distortions and in terms of the pronounced acceleration of the decay of the second excited state compared to that of the first excited state. We attribute that acceleration to the break-down of the adiabatic approximation for the second excited state. The adiabatic approximation is in fact implicitly always used when we think of the vibrational spectroscopy of the OH/OD vibration involved in an hydrogen bond. However, under the assumption of the Lippincott-Schroeder potential, the second excited state lives for only half a vibrational period of the O···O vibration. As such, we would conclude that it becomes essentially meaningless to talk about a second excited state of the OD vibration, because that state is strongly mode-mixed with lattice degrees of freedom. In accordance with earlier work,[10,11] we find however that the adiabatic picture is still quite correct for the first excited state, where the effect of anharmonicity is much smaller. A similar crossover behavior has been observed in models of vibrational energy flow in polyatomic molecules, where a transition between a localized energy flow regime at low excitations to a highly delocalized and facile regime at higher energies has been observed.[79,80]

The Lippincott-Schroeder potential is an empirical potential, which has been proposed based on the observed redshift of the OH vibration in hydrogen-bonded molecular crystals, that increases with decreasing O···O intermolecular distance.[64] Its functional form Eq. (1) is motivated by the chemical intuition that the proton may bind to either the hydrogen-bond donor or the acceptor, where one would have an auto-ionized state of water $OH^-\cdots H_3O^+$ in the latter case.

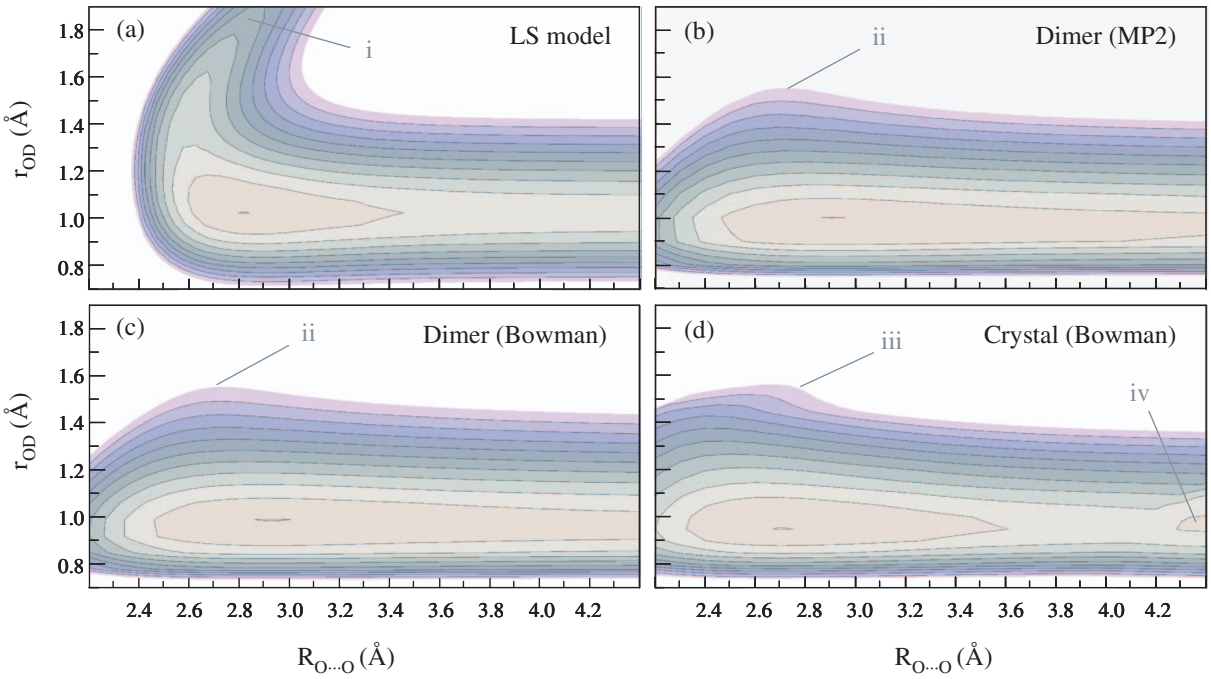

FIG. 8. Comparison of (a) the Lippincott-Schroeder potential with *ab initio* based potentials of the water dimer (b,c) in vacuum and (d) in an ice Ih crystal. Labels i-iv indicate features discussed in the text.

A fit of the OH frequency in dependence of the O···O distance for a series of hydrogen-bonded molecular crystals resulted in its parametrization. To the best of our knowledge, however, the Lippincott-Schroeder potential has never been thoroughly verified against *ab initio* calculations (one step in this direction is found in Ref. 81).

A comparison of the Lippincott-Schroeder model to various levels of *ab initio* based potential is shown in Fig. 8 (see Sec. III for details). The turnover feature of the Lippincott-Schroeder model for small r_{OD}'s (label i in Fig. 8(a)) reflects the auto-ionized $HO^-\cdots DOH_2^+$ state and is indeed reproduced partially in the case of a water-dimer in vacuum, but much less pronounced and at higher energies, by both a MP2/aug-cc-pVTZ treatment[65] (label ii in Fig. 8(b)) or when employing a parameterized potential by Bowman and coworkers (label ii in Fig. 8(c)).[66,67] When placing the dimer into a crystal environment, which adds both electronic and orientational polarizability that could in principle stabilize (solvate) the auto-ionized state, this feature becomes a bit more pronounced (label iii in Fig. 8(d)), but still not quite at the level of the Lippincott-Schroeder potential. Also the very steep rise of the Lippincott-Schroeder potential for low O···O distances (which originates from the Morse term V_{II} in Eq. (1)) is not reproduced. In fact, the anharmonicity of either one of the *ab initio* potentials is too small, and all of them fail to reproduce the 3D-IR lineshape distortions as well as the observed fast decay of the second excited state.

This leaves us with the question why the Lippincott-Schroeder model is capable to describe the nonlinear spectroscopy so well. Either the quantum chemistry misses an important aspect of the potential (which we do not consider to be very likely), or we need to think of the Lippincott-Schroeder potential as an effective potential that lumps the multidimensional character of the problem into one effective intermolecular degree of freedom that we call $R_{O\cdots O}$. In this regard it is interesting to note that the Lippincott-Schroeder potential has been fit to reproduce the red-shift of the OH vibrational frequency in dependence of the O···O distance, which is one aspect of anharmonic coupling, but here, we explore a very different aspect of anharmonicity, i.e., its consequence for nonadiabatic effects. We nonetheless get very good agreement which we find quite remarkable. Clarifying this question will require multidimensional quantum dynamics simulations, which are beyond the scope of this paper.

As a final remark, in the case of the crystal a second minimum appears at O···O distances longer than 4.2 Å (label iv in Fig. 8(d)), which corresponds to case where the hydrogen-bond is broken and the two waters that have entered the neighboring cages as interstitial waters. The barrier for this transformation (2800 cm^{-1}) is similar to the hydrogen bond dissociation energy in the Lippincott-Schroeder potential. Assuming that nonadiabatic effects can indeed funnel energy specifically into the $R_{O\cdots O}$ coordinate, as suggested in Fig. 7, this observation would open the possibility to prepare a crystal defect by vibrational excitation.

ACKNOWLEDGMENTS

We would like to thank Gerhard Stock, Julien Réhault, Paul Donaldson, and Sean Garrett-Roe for the very helpful comments. Furthermore, we thank Joel Bowman for discussions and for making his potential energy surface of water available. This work has been supported by the Swiss National Science Foundation (SNF) through the NCCR MUST.

[1] K. L. Vodopyanov, J. Chem. Phys. **94**, 5389–5393 (1991).
[2] S. Woutersen, U. Emmerichs, and H. J. Bakker, Science **278**(5338), 658–660 (1997).

[3]R. Laenen, C. Rauscher, and A. Laubereau, Phys. Rev. Lett. **80**(12), 2622 (1998).
[4]G. M. Gale, G. Gallot, F. Hache, N. Lascoux, S. Bratos, and J.-C. Leicknam, Phys. Rev. Lett. **82**(5), 1068–1071 (1999).
[5]Z. Wang, A. Pakoulev, Y. Pang, and D. D. Dlott, J. Phys. Chem. A **108**(42), 9054–9063 (2004).
[6]T. Steinel, J. B. Asbury, J. Zheng, and M. D. Fayer, J. Phys. Chem. A **108**, 10957–10964 (2004).
[7]D. Schwarzer, J. Lindner, and P. Vöhringer, J. Chem. Phys. **123**(16), 161105 (2005).
[8]J. Lindner, P. Vöhringer, M. S. Pshenichnikov, D. Cringus, D. A. Wiersma, and M. Mostovoy, Chem. Phys. Lett. **421**(4–6), 329–333 (2006).
[9]S. Ashihara, N. Huse, A. Espagne, E. T. J. Nibbering, and T. Elsaesser, J. Phys. Chem. A **111**, 743–746 (2007).
[10]A. Staib and J. T. Hynes, Chem. Phys. Lett. **204**, 197–205 (1993).
[11]R. Rey, K. B. Moller, and J. T. Hynes, Chem. Rev. **104**, 1915–1928 (2004).
[12]C. P. Lawrence and J. L. Skinner, J. Chem. Phys. **117**, 8847–8854 (2002).
[13]M. L. Cowan, B. D. Bruner, N. Huse, J. R. Dwyer, B. Chugh, E. T. J. Nibbering, T. Elsaesser, and R. J. D. Miller, Nature (London) **434**, 199–202 (2005).
[14]D. Kraemer, M. L. Cowan, A. Paarmann, N. Huse, E. T. J. Nibbering, T. Elsaesser, and R. J. D. Miller, Proc. Natl. Acad. Sci. U.S.A. **105**(2), 437–442 (2008).
[15]J. Stenger, D. Madsen, P. Hamm, E. T. J. Nibbering, and T. Elsaesser, Phys. Rev. Lett. **87**(2), 027401 (2001).
[16]S. Yeremenko, M. S. Pshenichnikov, and D. A. Wiersma, Chem. Phys. Lett. **369**(1–2), 107–113 (2003).
[17]C. J. Fecko, J. D. Eaves, J. J. Loparo, A. Tokmakoff, and P. L. Geissler, Science **301**, 1698–1702 (2003).
[18]J. B. Asbury, T. Steinel, K. Kwak, S. A. Corcelli, C. P. Lawrence, J. L. Skinner, and M. D. Fayer, J. Chem. Phys. **121**, 12431–12446 (2004).
[19]J. D. Eaves, J. J. Loparo, C. J. Fecko, S. T. Roberts, A. Tokmakoff, and P. L. Geissler, Proc. Natl. Acad. Sci. U.S.A. **102**(37), 13019–13022 (2005).
[20]F. Perakis and P. Hamm, J. Phys. Chem. B **115**, 5289–5293 (2011).
[21]R. A. Nicodemus, S. A. Corcelli, J. L. Skinner, and A. Tokmakoff, J. Phys. Chem. B **115**(18), 5604–5616 (2011).
[22]E. T. J. Nibbering and T. Elsaesser, Chem. Rev. **104**, 1887–1914 (2004).
[23]S. T. Roberts, K. Ramasesha, and A. Tokmakoff, Acc. Chem. Res. **42**, 1239–1249 (2009).
[24]T. Elsaesser, Acc. Chem. Res. **42**, 1220–1228 (2009).
[25]T. Yagasaki and S. Saito, Acc. Chem. Res. **42**(9), 1250–1258 (2009).
[26]H. J. Bakker and J. L. Skinner, Chem. Rev. **110**(3), 1498–1517 (2010).
[27]C. G. Salzmann, P. G. Radaelli, E. Mayer, and J. L. Finney, Phys. Rev. Lett. **103**, 105701 (2009).
[28]T. Loerting, K. Winkel, M. Seidl, M. Bauer, C. Mitterdorfer, P. H. Handle, C. G. Salzmann, E. Mayer, J. L. Finney, and D. T. Bowron, Phys. Chem. Chem. Phys. **13**, 8783–8794 (2011).
[29]P. V. Hobbs, *Ice Physics* (Oxford University Press, Oxford, 1974).
[30]C. Bäktorp, J. A. Poulsen, and G. Nyman, J. Phys. Chem. A **109**(14), 3105–3110 (2005).
[31]F. Li and J. L. Skinner, J. Chem. Phys. **133**, 244504 (2010).
[32]T. Yagasaki and S. Saito, J. Chem. Phys. **135**(24), 244511 (2011).
[33]L. Shi, S. M. Gruenbaum, and J. L. Skinner, J. Phys. Chem. B **116**(47), 13821–13830 (2012).
[34]R. Laenen, C. Rauscher, and A. Laubereau, J. Phys. Chem. B **102**(46), 9304–9311 (1998).
[35]F. Perakis and P. Hamm, Phys. Chem. Chem. Phys. **14**, 6250–6256 (2011).
[36]G. Seifert, K. Weidlich, and H. Graener, Phys. Rev. B **56**, R14231 (1997).
[37]S. Woutersen, U. Emmerichs, H. Nienhuys, and H. J. Bakker, Phys. Rev. Lett. **81**, 1106 (1998).
[38]A. M. Dokter and H. J. Bakker, J. Chem. Phys. **128**, 024502 (2008).
[39]R. L. A. Timmer and H. J. Bakker, J. Phys. Chem. A **114**, 4148–4155 (2010).
[40]F. Perakis, S. Widmer, and P. Hamm, J. Chem. Phys. **134**, 204505 (2011).
[41]H. Iglev, M. Schmeisser, K. Simeonidis, A. Thaller, and A. Laubereau, Nature (London) **439**, 183–186 (2006).
[42]Y. Marechal and A. Witkowski, J. Chem. Phys. **48**, 3697–3705 (1968).
[43]P. Hamm and M. T. Zanni, *Concepts and Methods of 2D Infrared Spectroscopy* (Cambridge University Press, Cambridge, 2011).
[44]R. R. Ernst, Angew. Chem., Int. Ed. **31**, 805–823 (1992).
[45]D. B. Turner, K. W. Stone, K. Gundogdu, and K. A. Nelson, J. Chem. Phys. **131**, 144510 (2009).
[46]J. A. Davis, C. R. Hall, L. V. Dao, K. A. Nugent, H. M. Quiney, H. H. Tan, and C. Jagadish, J. Chem. Phys. **135**, 044510 (2011).
[47]X. Dai, M. Richter, H. Li, A. D. Bristow, C. Falvo, S. Mukamel, and S. T. Cundiff, Phys. Rev. Lett. **108**, 193201 (2012).
[48]A. F. Fidler, E. Harel, and G. S. Engel, J. Phys. Chem. Lett. **1**(19), 2876–2880 (2010).
[49]Z. Zhang, K. L. Wells, and H.-S. Tan, Opt. Lett. **37**(24), 5058–5060 (2012).
[50]E. C. Fulmer, F. Ding, P. Mukherjee, and M. T. Zanni, Phys. Rev. Lett. **94**, 067402 (2005).
[51]F. Ding and M. T. Zanni, Chem. Phys. **341**(1–3), 95–105 (2007).
[52]S. Garrett-Roe and P. Hamm, J. Chem. Phys. **130**, 164510–9 (2009).
[53]S. Garrett-Roe and P. Hamm, Acc. Chem. Res. **42**, 1412–1422 (2009).
[54]S. Garrett-Roe, F. Perakis, F. Rao, and P. Hamm, J. Phys. Chem. B **115**, 6976 (2011).
[55]M. Khalil, N. Demirdöven, and A. Tokmakoff, Phys. Rev. Lett. **90**(4), 047401 (2003).
[56]J. C. Kirkwood, D. J. Ulness, and A. C. Albrecht, J. Phys. Chem. A **104**(18), 4167–4173 (2000).
[57]P. M. Donaldson, R. Guo, F. Fournier, E. M. Gardner, L. M. C. Barter, C. J. Barnett, I. R. Gould, D. R. Klug, D. J. Palmer, and K. R. Willison, J. Chem. Phys. **127**(11), 114513 (2007).
[58]J. C. Wright, Annu. Rev. Phys. Chem. **62**, 209–230 (2011).
[59]P. Hamm, R. A. Kaindl, and J. Stenger, Opt. Lett. **25**, 1798 (2000).
[60]V. Volkov, R. Schanz, and P. Hamm, Opt. Lett. **30**(15), 2010–2012 (2005).
[61]E. H. G. Backus, S. Garrett-Roe, and P. Hamm, Opt. Lett. **33**(22), 2665–2667 (2008).
[62]C. T. Middleton, D. B. Strasfeld, and M. T. Zanni, Opt. Express **17**(17), 14526–14533 (2009).
[63]R. Bloem, S. Garrett-Roe, H. Strzalka, P. Hamm, and P. Donaldson, Opt. Express **18**, 27067–27078 (2010).
[64]E. R. Lippincott and R. Schroeder, J. Chem. Phys. **23**, 1099 (1955).
[65]M. J. Frisch, G. W. Trucks, H. B. Schlegel *et al.*, GAUSSIAN 09, Revision A.1, Gaussian Inc., Wallingford, CT, 2009.
[66]Y. Wang, B. C. Shepler, B. J. Braams, and J. M. Bowman, J. Chem. Phys. **131**(5), 054511 (2009).
[67]Y. Wang, X. Huang, B. C. Shepler, B. J. Braams, and J. M. Bowman, J. Chem. Phys. **134**(9), 094509-1–094509-12 (2011).
[68]H. Liu, Y. Wang, and J. M. Bowman, J. Phys. Chem. Lett. **3**, 3671–3676 (2012).
[69]A. R. Leach, *Molecular Modelling, Principles and Applications* (Pearson Education Limited, Essex, England, 2001).
[70]G. C. Groenenboom and D. T. Colbert, J. Chem. Phys. **99**(12), 9681–9696 (1993).
[71]S. Mukamel, *Principles of Nonlinear Optical Spectroscopy* (Oxford University Press, Oxford, 1995).
[72]S.-C. Park, K.-H. Jung, and H. Kang, J. Chem. Phys. **121**(6), 2765–2774 (2004).
[73]J. C. Werhahn, S. Pandelov, S. S. Xantheas, and H. Iglev, J. Phys. Chem. Lett. **2**(13), 1633–1638 (2011).
[74]H. J. Bakker and H. Nienhuys, Science **297**, 587–590 (2002).
[75]B. S. Alexandrov, V. G. Stanev, A. R. Bishop, and K. Rasmussen, Phys. Rev. E **86**(6), 061913 (2012).
[76]M. Gühr, M. Bargheer, and N. Schwentner, Phys. Rev. Lett. **91**(8), 085504 (2003).
[77]C. P. Lawrence and J. L. Skinner, J. Chem. Phys. **119**(3), 1623–1633 (2003).
[78]D. J. Nesbitt and R. W. Field, J. Phys. Chem. **100**(31), 12735–12756 (1996).
[79]R. Marquardt and M. Quack, J. Chem. Phys. **95**(7), 4854–4876 (1991).
[80]M. Gruebele and P. G. Wolynes, Acc. Chem. Res. **37**, 261–267 (2004).
[81]M. V. Vener, Chem. Phys. Lett. **244**, 89–92 (1995).